ULTRA
SONO
GRAPHY

Intravascular ultrasound imaging with directional synthetic aperture focusing and coherence factor weighting

ORIGINAL ARTICLE

https://doi.org/10.14366/usg.25061
eISSN: 2288-5943
Ultrasonography 2025;44:483-499

Hyunwoo Cho[1]*, Jaebin Lee[1]*, Daehyun Park[1], Jin Ho Chang[2], Jihun Jang[3,4], Yangmo Yoo[1,3,4]

[1]Department of Electronic Engineering, Sogang University, Seoul; [2]Department of Information and Communication Engineering, Daegu Gyeongbuk Institute of Science and Technology, Daegu; [3]Department of Biomedical Engineering, Sogang University, Seoul; [4]Medical Solution Institute, Sogang University, Seoul, Korea

Purpose: Intravascular ultrasound (IVUS) is widely used to visualize vascular structures and assess atherosclerotic plaques, particularly for evaluating the risk of rupture. Although increasing the center frequency of the transducer can enhance spatial resolution, it also increases attenuation, which substantially degrades image quality at greater depths. To mitigate this trade-off, synthetic aperture focusing (SAF) techniques have been studied; however, when applied to single-element rotational IVUS systems, they have yielded only minimal improvements and introduced undesirable artifacts.

Methods: In this work, a directional SAF (dSAF) method is proposed to address these limitations. The convex nature of the point spread function in rotational IVUS scanning is analyzed to track the true direction of echo signals, enabling the selective exclusion of off-axis signals. By focusing only on valid signals during synthesis, resolution degradation and artifact formation are prevented, and the fidelity of the reconstructed image is preserved.

Results: Validation through simulations and phantom experiments indicates that the dSAF method achieves an average 37.3% improvement in lateral resolution and an 8.6% increase in contrast-to-noise ratio, without degrading penetration depth.

Conclusion: These findings suggest that directional echo screening effectively mitigates the limitations encountered with conventional SAF in IVUS imaging, offering a robust pathway to improved image quality. Additionally, the proposed approach can be integrated into existing IVUS workflows, potentially expediting clinical adoption and advancing intravascular diagnostic capabilities.

Keywords: Coherence factor weighting; Directional map; Echo directional analysis; Intravascular ultrasound; Synthetic aperture focusing

Key points: The directional synthetic aperture focusing (dSAF) method leverages the convex point spread function characteristics in rotational intravascular ultrasound (IVUS) to selectively synthesize valid echo signals, thereby reducing resolution degradation and preventing artifact formation. Simulations and phantom experiments demonstrate that dSAF improves lateral resolution by an average of 37.3% and increases contrast-to-noise ratio by 8.6% without compromising penetration depth. This approach can be seamlessly integrated into existing IVUS workflows, potentially accelerating clinical adoption and enhancing intravascular diagnostic capabilities.

Received: April 13, 2025
Revised: September 3, 2025
Accepted: September 8, 2025

Correspondence to:
Yangmo Yoo, PhD, Department of Electronic Engineering, Sogang University, 35 Baekbeom-ro, Mapo-gu, Seoul 04107, Korea

Tel. +82-2-705-8907
Fax. +82-2-707-3008
E-mail: ymyoo@sogang.ac.kr

*These authors contributed equally to this work.

How to cite this article:
Cho H, Lee J, Park D, Chang JH, Jang J, Yoo Y. Intravascular ultrasound imaging with directional synthetic aperture focusing and coherence factor weighting. Ultrasonography. 2025 Nov;44(6):483-499.

Introduction

Atherosclerotic cardiovascular disease is a major global health concern, with plaque rupture and subsequent thrombosis identified as critical factors underlying myocardial infarction and stroke [1,2]. Plaques characterized by a thin fibrous cap (<65 μm) and a large lipid core are highly vulnerable to rupture, posing a significant risk of acute events. Early and accurate identification of such lesions is essential for timely clinical intervention. Among various diagnostic techniques, intravascular ultrasound (IVUS) has become a preferred modality for providing cross-sectional images of vessel walls to assess plaque burden, luminal dimensions, and plaque composition [3,4].

Despite the widespread use of IVUS in interventional cardiology, its spatial resolution remains insufficient for measuring critical structures on the scale of tens of micrometers, such as thin fibrous caps. Conventional IVUS systems, often operating at center frequencies of 20–40 MHz, balance penetration depth against spatial resolution. However, this compromise frequently proves inadequate for visualizing the finer details associated with plaque vulnerability [5,6]. A straightforward way to enhance resolution is to raise the center frequency to 60 MHz or beyond, which narrows the acoustic beam and better resolves small targets [7]. Yet higher frequencies exacerbate frequency-dependent attenuation, leading to poor image quality in deeper regions and limiting the overall utility for comprehensive vessel wall assessment [8].

To address this trade-off, researchers have explored multi-frequency IVUS transducers that transmit and receive over different frequency bands. Low-frequency channels target deeper structures and maintain penetration, whereas high-frequency channels capture near-field or superficial plaque details [9–12]. While promising, these designs are challenging to fabricate and miniaturize, especially since the catheter in human coronary applications often must fit within a 1-mm diameter. Moreover, coupling multiple frequency bands typically requires complex cable assemblies and specialized back-end electronics, increasing both cost and design complexity.

Another major line of research involves nonlinear imaging approaches such as tissue harmonic imaging (THI). By leveraging harmonics generated through tissue nonlinearity, THI can improve lateral resolution and suppress sidelobes compared with fundamental imaging [13,14]. In IVUS, however, partitioning the bandwidth between the fundamental and harmonic components can degrade axial resolution unless wideband or dual-layer transducer designs are used [10,11,15–21]. These added complexities are likewise non-trivial to implement in a small-diameter catheter setting.

Recently, synthetic aperture focusing (SAF) and coherence factor weighting (CFW) have gained attention as purely signal-processing approaches for enhancing resolution and contrast in ultrasound imaging [22–32]. Several studies have introduced the fundamentals of SAF for array-based scanning, demonstrating significant improvements in image quality by coherently summing multiple low-energy transmissions [22–25]. Subsequent research [26–28] refined these approaches with CFW, which further suppresses off-axis noise and sidelobes by weighting each focal point according to the coherence of the received signals. Although these methods have produced encouraging results for linear array and two-dimensional array imaging, more recent studies [29–32] have explored adapting SAF and CFW to single-element, rotating IVUS transducers, recognizing that the limited aperture, rotational geometry, and distinct beam profile pose challenges distinct from array-based systems. Consequently, while conventional SAF (cSAF) can achieve focal gain comparable to that of a large aperture, its application to rotating IVUS remains non-trivial and can introduce artifacts if off-axis echoes are not carefully screened.

In a single-element rotational IVUS catheter, the transducer mechanically scans in a circular pattern. Because of the limited aperture and the characteristic beam profile about the rotational axis, cSAF offers only modest improvements in lateral resolution and may even degrade image quality by introducing artifacts [22,29,32]. One primary reason is that standard cSAF relies solely on time-of-flight calculations for each imaging point, ignoring whether each delayed echo truly originates from the on-axis region of interest. Off-axis reflectors, particularly if hyperechoic, may contaminate the summation and produce spurious bright regions. This phenomenon is exacerbated by the decreasing number of overlapping scanlines at greater radial distances, where beam spreading reduces the effective aperture [33].

To overcome these limitations, this article proposes a directional SAF (dSAF) method that selectively rejects invalid off-axis echoes by incorporating echo-directional information into beamforming. Specifically, the approach exploits the convex point spread function (PSF) pattern characteristic of rotational IVUS to determine the phase distribution of echoes across adjacent scanlines. By applying lag-1 autocorrelation to the in-phase and quadrature components, we compute a directional map indicating whether each echo arrives from a direction consistent with the desired on-axis target. Invalid echoes with phase trajectories that do not match the expected pattern are then excluded from the summation, thereby mitigating the artifacts often observed with cSAF. The authors further integrate CFW into dSAF (dSAF-CFW) to enhance contrast and sidelobe suppression, enabling flexible adaptation to different imaging needs.

The key contributions of this study can be summarized as follows: (1) Directional map for rotational IVUS: The authors develop a phase-based directional map tailored to the convex wavefronts in single-element rotational IVUS systems, enabling accurate identification of on-axis echoes. (2) Adaptive echo screening in SAF: The authors introduce a screening mask that excludes off-axis echoes during SAF, significantly reducing artifacts and enhancing lateral resolution. (3) Enhanced spatial and contrast resolution: In simulations and phantom experiments, the proposed method yields up to a 37.3% improvement in lateral resolution and an 8.6% increase in contrast-to-noise ratio (CNR), without compromising penetration depth.

Materials and Methods

Echo Directional Analysis

An echo distribution analysis was performed using a single-point-target model to investigate how echo signals shift across adjacent scanlines in IVUS imaging. As illustrated in Fig. 1A, the IVUS transducer was assumed to rotate about the origin, transmitting plane waves (red arrow) and receiving spherically propagating echoes (blue arrow). The echo traces from a point target at the center scanline (Fig. 1B) form a convex distribution, with the center scanline representing the minimal path length. Consequently, when the scanline shifts to the right, echoes on the left side of the center scanline move farther from the transducer, whereas echoes on the right side move closer.

These observations can be interpreted in terms of phase changes. As shown by the red and blue solid lines in Fig. 1C, adjacent echoes can exhibit either a phase lead or a phase lag relative to the center scanline signal. This phase relationship indicates whether an echo originates from an on-axis point target. Notably, the signs of valid phase changes depend on the scanning motion. In the rotational scan, the left and right sides of the on-axis scanline show lag (−) and lead (+), respectively (Fig. 1D). During a rightward linear B-scan, the far-field region displays the opposite sign pattern because beyond the focus, the local wavefront curvature reverses. As summarized in Fig. 1E, dSAF retains only phase-consistent contributions and suppresses opposite-sign ones. These differences arise from the echo-distribution geometry: rotational scanning yields a convex pattern, whereas linear scanning in the far field results in a concave pattern.

To quantify these directional phase changes, lag-1 autocorrelation [34] was applied to the in-phase (I) and quadrature-phase (Q) components along the scanline direction. The imaginary part (R_x) and the real part (R_y) of the lag-1 autocorrelation can be calculated as follows:

$$(R_x\,[s,n]=\sum_{i=-\frac{E}{2}}^{\frac{E}{2}-1}(I_{s+i}\,[n]\cdot Q_{s+i+1}\,[n]-I_{s+i+1}\,[n]\cdot Q_{s+i}\,[\mathrm{n}] \tag{1}$$

$$(R_y\,[s,n]=\sum_{i=\frac{E}{2}}^{\frac{E}{2}-1}(I_{s+i}\,[n]\cdot I_{s+i+1}\,[n]+Q_{s+i}\,[n]\cdot Q_{s+i+1}\,[\mathrm{n}] \tag{2}$$

$$D[s,n]=\tan^{-1}\left(\frac{R_x\,[s,n]}{R_y\,[s,n]}\right) \tag{3}$$

where s is the scanline index, E is the number of ensembles used to calculate the phase change, and n is the sample number. I and Q represent the in-phase and quadrature-phase signals of the scanline, respectively. The result of lag-1 autocorrelation, $D[s,n]$, is defined as the echo directional map.

An example of this echo directional map is shown in Fig. 1D, where the red and blue regions indicate echoes moving closer to and farther from the transducer, respectively. By comparing the observed phase changes in $D[s,n]$ with the expected phase signs for a desired scanline, invalid echoes originating from off-axis targets can be excluded. Further details regarding the identification of valid signals are provided in Section B, which uses a model with two adjacent point targets as an illustrative example.

dSAF and dSAF with CFW

cSAF and CFW

cSAF is typically implemented as the coherent summation of delayed scanline data:

$$S_{SAF}\,(s,t)=\sum_{i=-\frac{N}{2}}^{\frac{N}{2}}W_{apo}\,(s+i,t)\,S_{RF}\,(s+i,t-\Delta t_i) \tag{4}$$

where s denotes the scanline number, N represents the number of adjacent scanlines used for synthesis, S_{RF} indicates the scanline data, W_{apo} is an apodization weight, and Δt_i is the time-of-flight delay for each scanline at the desired imaging point [29].

CFW further refines resolution and contrast by down-weighting incoherent signals:

$$W_{\mathrm{CFW}}\,(s,t)=\frac{\left|\sum_{i=-\frac{N}{2}}^{\frac{N}{2}}S_{\mathrm{RF}}\,(s+i,t-\Delta t_i)\right|^2}{N\sum_{i=-\frac{N}{2}}^{\frac{N}{2}}\left|S_{\mathrm{RF}}\,(s+i,t-\Delta t_i)\right|^2} \tag{5}$$

and its result can be multiplied by $S_{SAF}\,(s,t)$ to obtain the cSAF-CFW image:

$$S_{\mathrm{SAF-CFW}}\,(s,t)=W_{\mathrm{CFW}}\,(s,t)\,S_{\mathrm{SAF}}\,(s,t) \tag{6}$$

dSAF

While cSAF and cSAF-CFW assume that all time-delayed echoes are valid, single-element IVUS imaging can suffer from off-axis targets that produce spurious echoes contributing to the on-axis scanline. To address this, a directional screening mask is introduced based on the echo directional map $D[s,n]$. This mask excludes echoes determined to have originated off-axis, preventing artifacts and

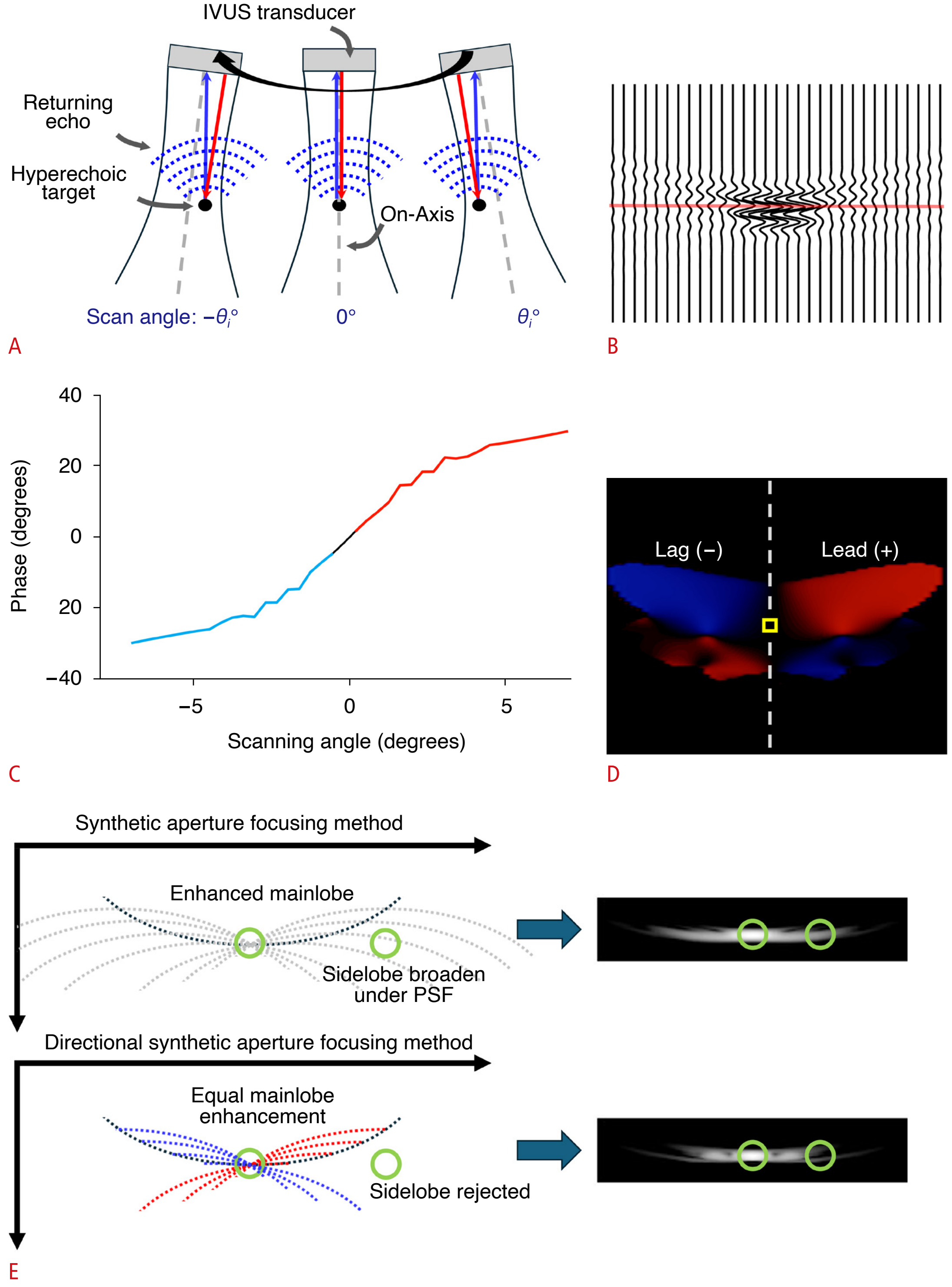

Fig. 1. Directional phase map and concept of directional synthetic aperture focusing in rotational intravascular ultrasound (IVUS). A. Illustration of the IVUS imaging scenario shows changes in scan angle. The curved arrow indicates the rotational motion of the transducer. The red arrow represents the transmit (TX) path of the beam, and the blue arrow denotes the receive (RX) path. B. Acquired echo traces from a point target located at the center scanline. C. Phase change was observed in adjacent scanlines at the depth indicated by the red solid line in B. D. Calculated phase change image of echo traces across all depths during the rotational scan is referred to as the echo directional map in this article. The blue and red regions represent lagging and leading phase changes in adjacent scanlines, respectively. E. Schematic of the proposed directional synthetic aperture focusing: phase-consistent contributions (same sign as the on-axis reference) are combined to enhance the mainlobe, while opposite-sign contributions are rejected. This mechanism also explains the opposite sign pattern in the far field of a rightward linear scan and the axial sign reversal across the focal region. PSF, point spread function.

improving lateral resolution.

The screening mask $M_{DMAP}(s,t,i)$ is computed by comparing the measured phase sign of $D(s+i,t-\Delta t_i)$ with the ideal sign expected for the desired scanline:

$$M_{DMAP}(s,t,i)=\begin{cases}\dfrac{-\operatorname{sgn}(D(s+i,t-\Delta t_i))+1}{2} & (i<0)\\ 1 & (i=0)\\ \dfrac{\operatorname{sgn}(D(s+i,t-\Delta t_i))+1}{2} & (i>0)\end{cases} \qquad (7)$$

where sgn is the sign function, i indexes the adjacent scanlines around the desired scanline s, and $i=0$ denotes the on-axis scanline, which is always considered valid.

By applying M_{DMAP} to Eqs. 4 and 6, the dSAF and dSAF-CFW images are generated:

$$S_{DSAF}(s,t)=\sum_{i=-\frac{N}{2}}^{\frac{N}{2}} M_{DMAP}(s,t,i)\,W_{Apo}(s,t,i)\,S_{RF}(s+i,t-\Delta t_i) \qquad (8)$$

$$S_{DSAF-CFW}(s,t)=W_{CFW}(s,t)\,S_{DSAF}(s,t) \qquad (9)$$

Fig. 2 contrasts the cSAF and dSAF procedures using two closely spaced point targets as an example. Figs. 2A-C depict how cSAF merges delayed radiofrequency (RF) scanlines (A-lines) from both on-axis and off-axis echoes, potentially generating interference artifacts. In contrast, Fig. 2D–F illustrate the calculation of the echo directional map via lag-1 autocorrelation (Eqs. 1–3) and the subsequent binarization step that retains only valid directional signals (Eq. 7). By synthesizing only these valid echoes, the dSAF method avoids off-axis contamination and achieves improved lateral resolution with fewer artifacts. As a result, the two closely

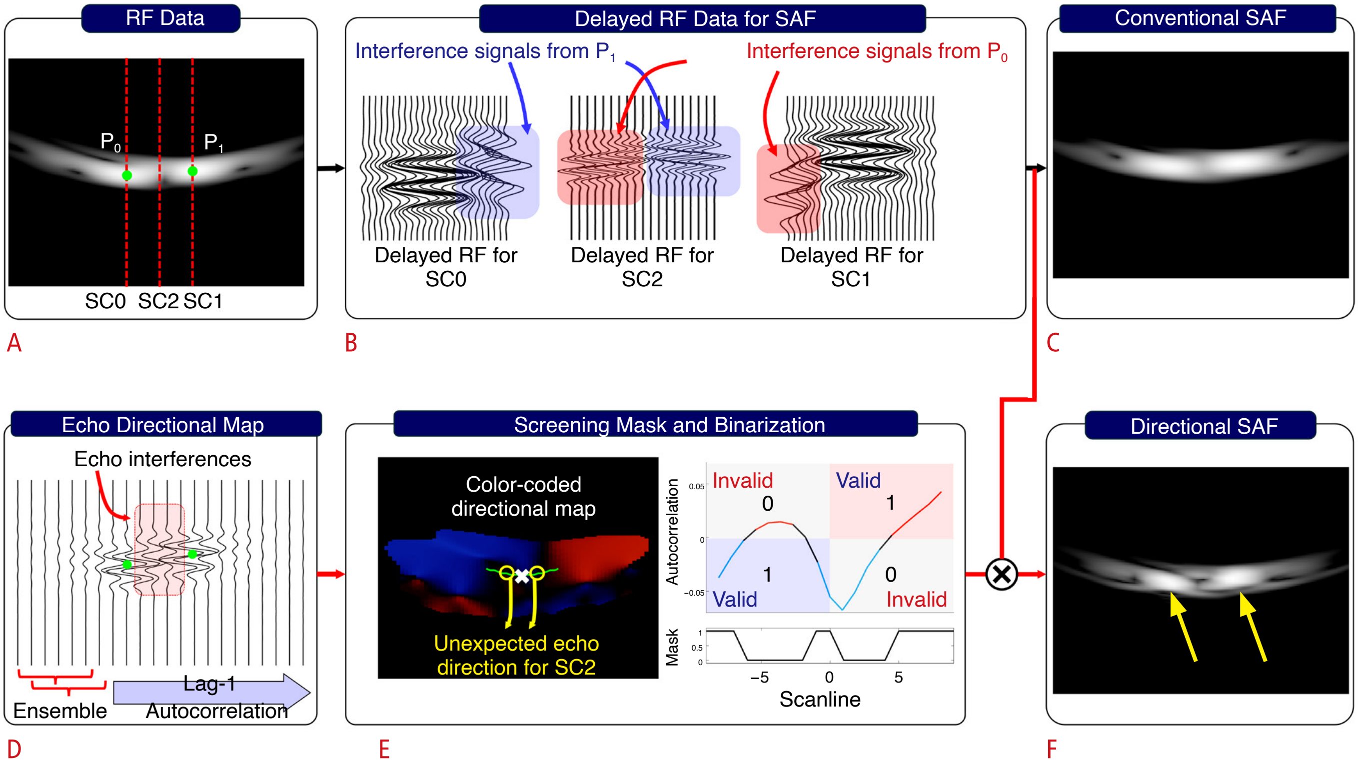

Fig. 2. **Flowchart comparing the conventional and proposed synthetic aperture focusing (SAF) processing methods.** The black arrow indicates the conventional SAF (cSAF) sequence, while the red arrow indicates the proposed sequence. A. Raw image of two targets (p0 and p1), depicted as green dots. B. Delayed radiofrequency (RF) data for SAF are shown at scanlines SC0, SC1, and SC2, as indicated in A. The shaded red and blue areas highlight the interference signals from point targets p0 and p1, respectively, when applying the SAF delay to each scanline. C. cSAF images were obtained through coherent summation of the delayed RF data. D. The echo directional map is calculated using lag-1 autocorrelation. E. Screening and binarization are achieved by comparing the estimated echo direction with the expected direction. Yellow circles highlight representative unexpected-echo locations for SC2 (opposite-sign) that are removed by the gate. F. Images are produced by the proposed method. The yellow arrows in F highlight that the two point targets are clearly separable after applying the proposed method, whereas the conventional method struggles to distinguish them.

spaced point targets are clearly separated in Fig. 2F, unlike in the conventional approach shown in Fig. 2C.

The proposed dSAF approach begins by computing a directional phase map via lag-1 autocorrelation between adjacent scanlines at each depth. The map is then binarized into a global gate (1=valid, 0=invalid) using a simple sign rule: a neighbor is valid when its phase sign matches the expected sign for that side of the on-axis scanline at the same depth, and invalid otherwise (applied to all neighbors and depths; Fig. 2E). For a given on-axis scanline, a binary gate mask is then constructed over neighboring scanlines using the same rule: phase-consistent neighbors are retained, and opposite-sign neighbors are excluded. The dSAF image is synthesized by delaying and summing only the retained RF scanlines; when CFW is applied, the surviving contributions are further weighted by their coherence, so near-zero or incoherent phases have negligible influence. The gate mask adapts with depth: when the sign pattern reverses beyond the focus, it follows the phase map, preventing post-focal opposite-sign energy from entering the aperture. In short, opposite-sign echoes are fully excluded by the binary gate, whereas phase-consistent echoes are included and, if incoherent, partially down-weighted by CFW.

Experimental setups

A field II simulation was performed prior to the experiments to validate the proposed approach. A flat rectangular transducer (0.5 mm×0.5 mm) with a center frequency of 54 MHz was modeled, and four-point targets were placed along the axial direction at depths of 2, 3, 4, and 5 mm. The transducer was rotated counterclockwise in 0.36° increments, yielding 1,000 scanlines per full rotation. Using the acquired RF data, images were reconstructed by applying cSAF, cSAF-CFW, dSAF, and dSAF-CFW, as described in Section B. The number of synthetic scanlines N was adjusted with depth to account for the beam distribution (for example, 39 at 2 mm and 15 at 5 mm), and seven ensembles were used to compute the echo directional map $D[s,n]$, reflecting beam overlap in rotational scanning. After beam synthesis, the images were envelope-detected, log-compressed (50 dB dynamic range), and scan-converted. Performance metrics in this simulation included lateral resolution (assessed by measuring the −6 dB beamwidth at each of the four point targets), axial resolution (obtained from the −6 dB beamwidth along each target's depth axis), and relative peak magnitude (the maximum intensity of the axial profile), used to assess whether penetration depth was compromised.

Phantom experiments, as shown in Fig. 3, were conducted to further validate the proposed method. For the wire phantom experiment, a 25-μm gold wire was suspended in a water tank and aligned with the same flat-aperture IVUS transducer (center frequency: 54 MHz, aperture: 0.5 mm×0.5 mm) used in the simulation study [6]. The transducer was mounted on a rotational stage (SGSP160-YAW, Sigmakoki Co. Ltd., Tokyo, Japan) that rotated counterclockwise in 0.36° increments, acquiring 1000 scanlines. Excitation and signal amplification were provided by a pulser/receiver (UT340, UTEX Scientific Instruments Inc., Mississauga, ON, Canada), and a high-speed digitizer (CS12502, Gage Applied Technologies Inc., Montreal, QC, Canada) captured the signals for offline processing. A custom tissue-mimicking phantom containing

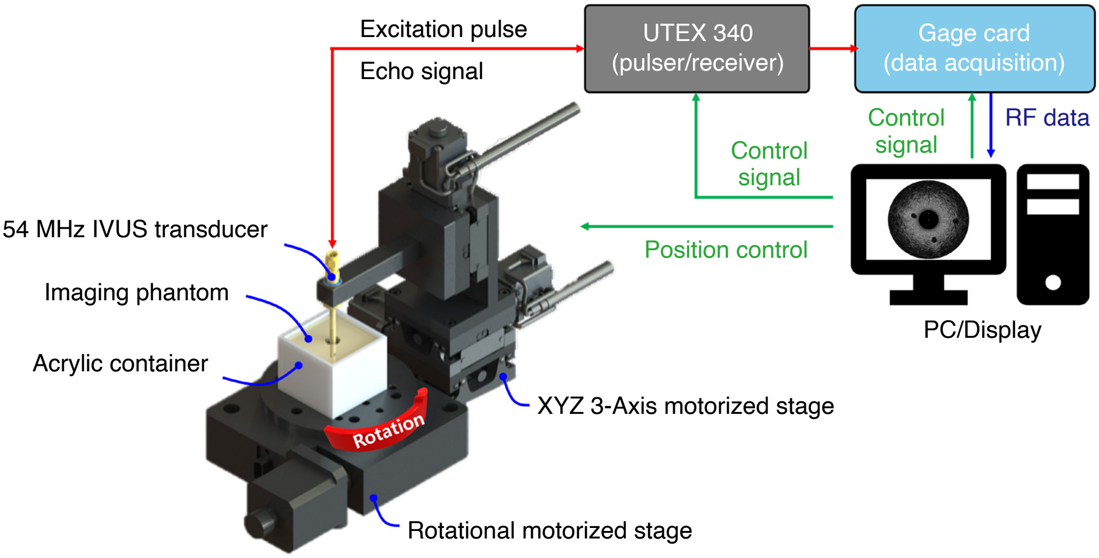

Fig. 3. **Illustration of the experimental setup to acquire intravascular ultrasound (IVUS) image data.** Radiofrequency (RF) data were collected as the rotary stage was rotated in 0.36° steps.

three cystic regions (~1 mm in diameter) was also prepared to assess contrast performance at depths of 2, 3, and 4 mm, using the same rotational imaging procedure and recording conditions. Further details regarding phantom fabrication were described previously [6]. All instruments, including the rotational stage and digitizer, were operated through a custom LabVIEW program. Post-processing steps such as beamforming, directional masking, and CFW were performed in MATLAB (MathWorks Inc., Natick, MA, USA) using the same parameters as in the simulation.

Lateral and axial resolutions, as well as penetration depth, were evaluated following the same procedures as in the simulation study. In addition, to quantify contrast performance in the tissue-mimicking phantom, the CNR was calculated as:

$$CNR=\frac{|\mu_{signal}-\mu_{background}|}{\sqrt{\sigma_{signal}^2+\sigma_{background}^2}} \tag{10}$$

where μ_{signal} and $\mu_{background}$ are the mean intensities of the signal (cystic region) and background, respectively, and σ_{signal} and $\sigma_{background}$ are their standard deviations. Higher CNR values indicate better contrast resolution.

Results

Simulation Study

To demonstrate the effectiveness of the proposed method, PSF imaging simulations were performed using Field II. A flat rectangular IVUS transducer (0.5 mm×0.5 mm) operating at a center frequency of 54 MHz was modeled, and four-point targets were positioned along the axial direction at depths of 2, 3, 4, and 5 mm. The targets were rotated counterclockwise around the origin in 0.36° increments, producing 1000 scanlines. Based on these scanline data, cSAF, cSAF-CFW, dSAF, and dSAF-CFW reconstructions were carried out as described previously, with the number of synthetic scanlines adjusted by depth to account for the radiation pattern (with 39, 27, 19, and 15 scanlines at 2, 3, 4, and 5 mm, respectively). For dSAF, seven ensembles were used to compute the echo directional map, reflecting beam overlap in rotational scanning. Following beam synthesis, envelope detection, logarithmic compression, and digital scan conversion were applied to each image, all of which were displayed with a 50-dB dynamic range.

Fig. 4 presents the resulting PSF images of the four wire targets. Fig. 4A depicts the conventional (raw) image, while Fig. 4B presents

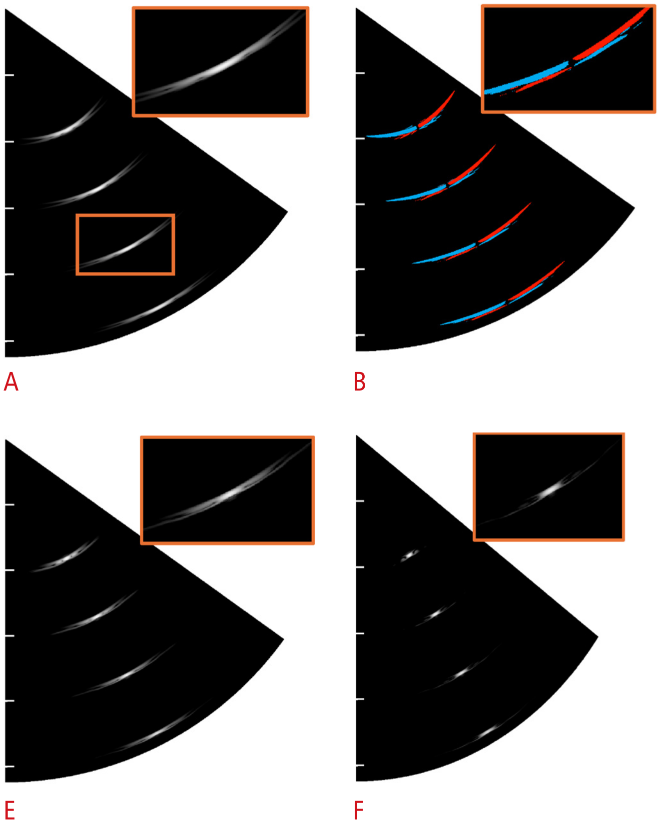

Fig. 4. Simulated point spread function images with four wire targets at 2, 3, 4, and 5 mm.
A. Conventional (raw) image is shown. B. The echo directional map is calculated based on scanline data acquired during rotation of the intravascular ultrasound transducer. Axial reversal of the phase sign (blue ↔ red with depth) appears as the beam passes the focal region: pre-focal depths follow the rotational pattern (left lag, right lead), whereas post-focal depths display the opposite pattern. Fig. 1E illustrates how directional synthetic aperture focusing (dSAF) uses this sign behavior to enhance phase-consistent energy and reject opposite-sign contributions. C, D. Conventional SAF (cSAF) (C) and cSAF with coherence factor weighting (CFW) (D) images are shown. E, F. dSAF (E) and dSAF-CFW (F) images are shown. All images were logarithmically compressed with a dynamic range of 50 dB. The white bar on the vertical axis indicates 1-mm intervals.

the calculated echo directional map. Fig. 4C and D show cSAF and cSAF-CFW images, respectively, while proposed dSAF and dSAF-CFW images are illustrated in Fig. 4E and F. As the figure indicates, cSAF and cSAF-CFW can enhance resolution at shallower depths but often degrade at 4 and 5 mm, where invalid off-axis echoes contaminate the on-axis synthesis.

To assess spatial resolution more quantitatively, −6 dB beamwidth measurements were performed in both lateral and axial directions at each target depth. Fig. 5 compares the lateral beam profiles for each method, while Fig. 6 shows the axial profiles. The lateral beamwidths of the raw image were 290, 196, 229, and 275 μm at 2, 3, 4, and 5 mm, respectively. In contrast, cSAF achieved narrower beamwidths (116, 178, 238, and 293 μm) at shallower depths but displayed noticeable degradation at greater depths, consistent with previous research [32]. The proposed dSAF approach further reduced the beamwidths to 84, 107, 130, and 156 μm at the same depths, corresponding to an average improvement of approximately 51.8% over the raw image and 42.2% over cSAF. This benefit is attributed to screening out off-axis echoes, which cSAF includes without verification.

CFW can be applied to further suppress sidelobes, as shown in Figs. 5 and 6. In cSAF-CFW, the lateral beamwidths were 71, 103,

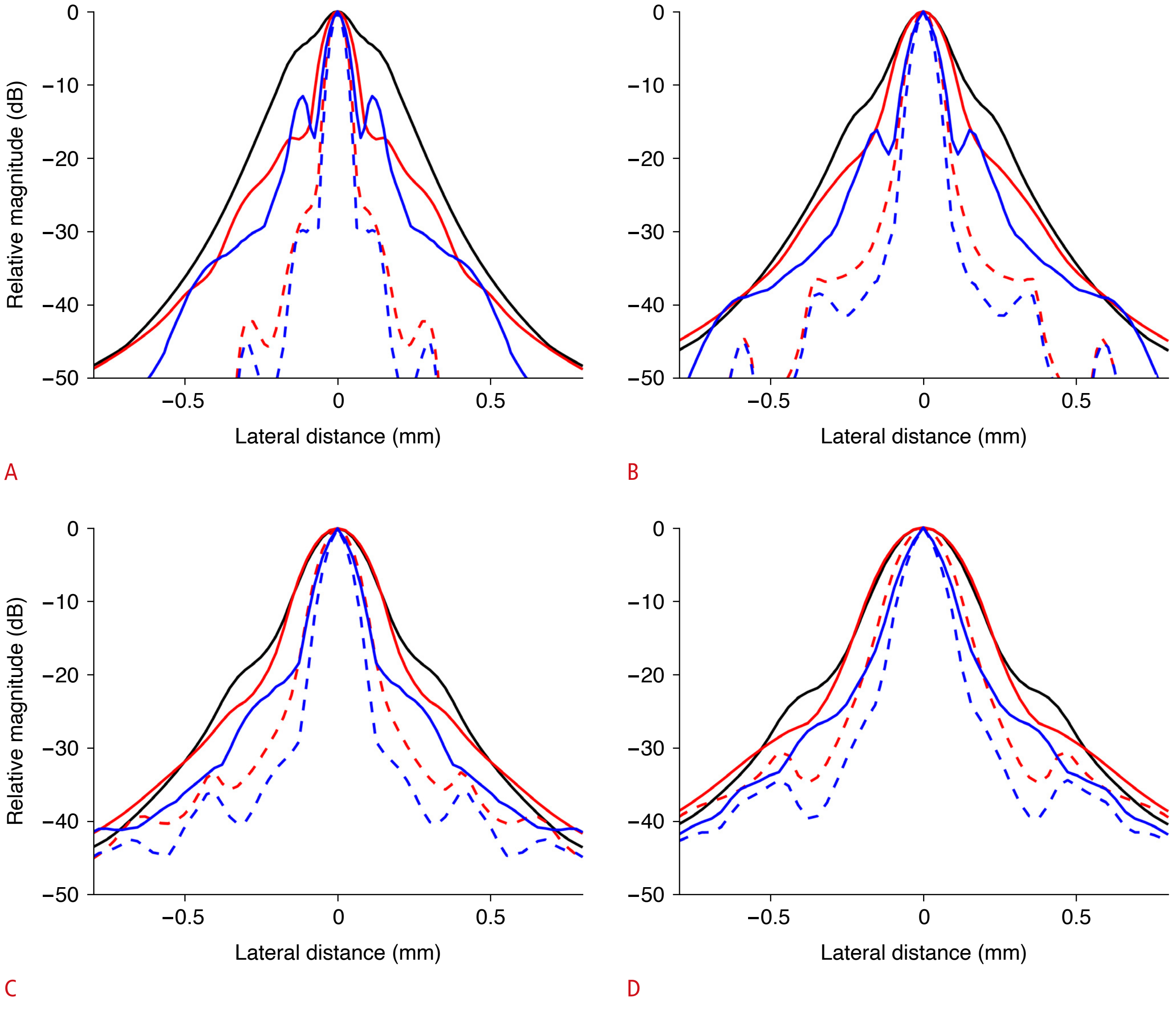

Fig. 5. Simulated lateral beam profiles at 2–5 mm.
A–D. Simulated lateral beam profiles of each method are shown at target positions of 2, 3, 4, and 5 mm, respectively. The solid black line represents the raw data; the solid and dotted red lines indicate conventional synthetic aperture focusing (cSAF) and cSAF-coherence factor weighting (CFW), respectively; and the solid and dotted blue lines denote directional SAF (dSAF) and dSAF-CFW, respectively.

144, and 200 μm, while dSAF-CFW yielded even smaller values of 62.6, 84.5, 109, and 135 μm—about a 24.5% improvement over cSAF-CFW. However, CFW can sometimes introduce overall gain reduction or dark region artifacts near strong reflectors, indicating that it may not always resolve the image quality issues faced by SAF. Notably, dSAF alone surpassed cSAF-CFW by roughly 16.8% at depths of 4 and 5 mm, suggesting potential clinical utility for high-definition IVUS images without the drawbacks of CFW.

Penetration depth was evaluated using the axial beam profiles in Fig. 6 and summarized data in Fig. 7. Although SAF tends to increase overall signal magnitude relative to the raw image, the peak magnitudes of dSAF closely matched those of cSAF across all depths. These findings suggest that dSAF does not compromise penetration depth, even though directional screening uses fewer scanlines. In other words, the proposed method preserves penetration while substantially enhancing lateral resolution, offering a favorable trade-off for rotational IVUS applications.

Fig. 7A further summarizes the −6 dB lateral beamwidths at 2, 3, 4, and 5 mm, and Fig. 7B shows the corresponding relative peak magnitudes. Taken together, these results confirm that dSAF and dSAF-CFW outperform cSAF methods in spatial resolution and penetrating power.

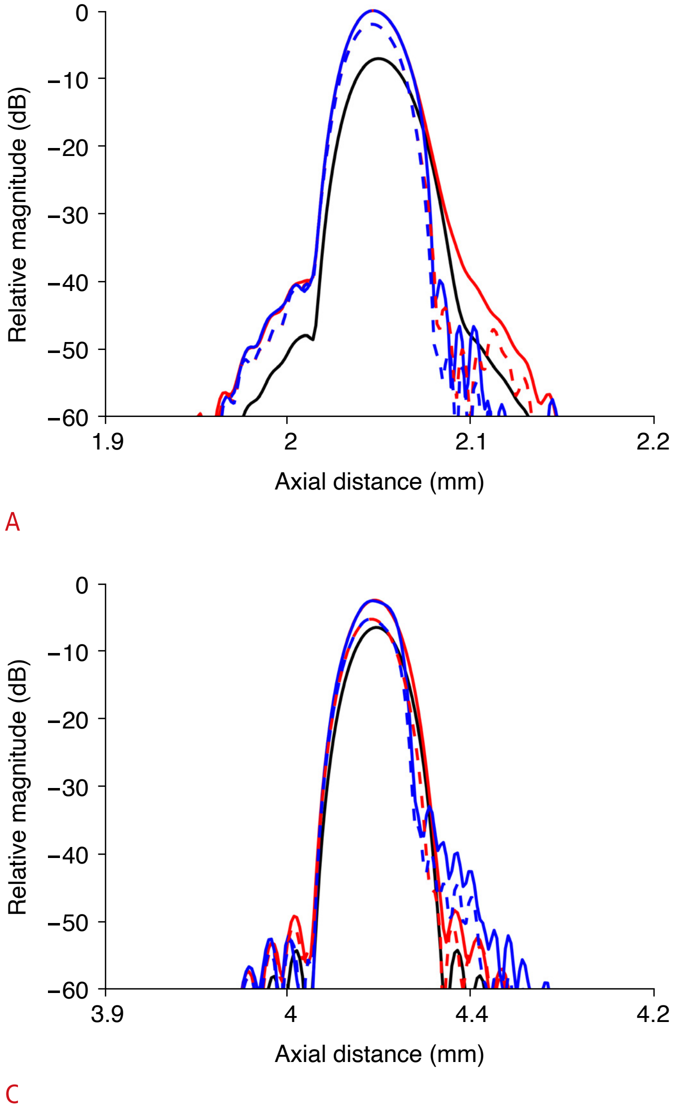

Fig. 6. Simulated axial beam profiles at 2–5 mm.

A–D. Simulated axial beam profiles of each method are shown at target positions of 2, 3, 4, and 5 mm, respectively. The solid black line represents the raw data, the solid and dotted red lines correspond to conventional synthetic aperture focusing (cSAF) and cSAF-coherence factor weighting (CFW), and the solid and dotted blue lines indicate directional SAF (dSAF) and dSAF-CFW, respectively.

Experimental Phantom Study

To validate the effectiveness of the proposed methods in a realistic setting, phantom experiments were conducted using a 25-μm gold wire target and a tissue-mimicking phantom. Detailed information regarding the target configurations and phantom preparation was presented previously [6]. A flat aperture transducer (0.5 mm×0.5

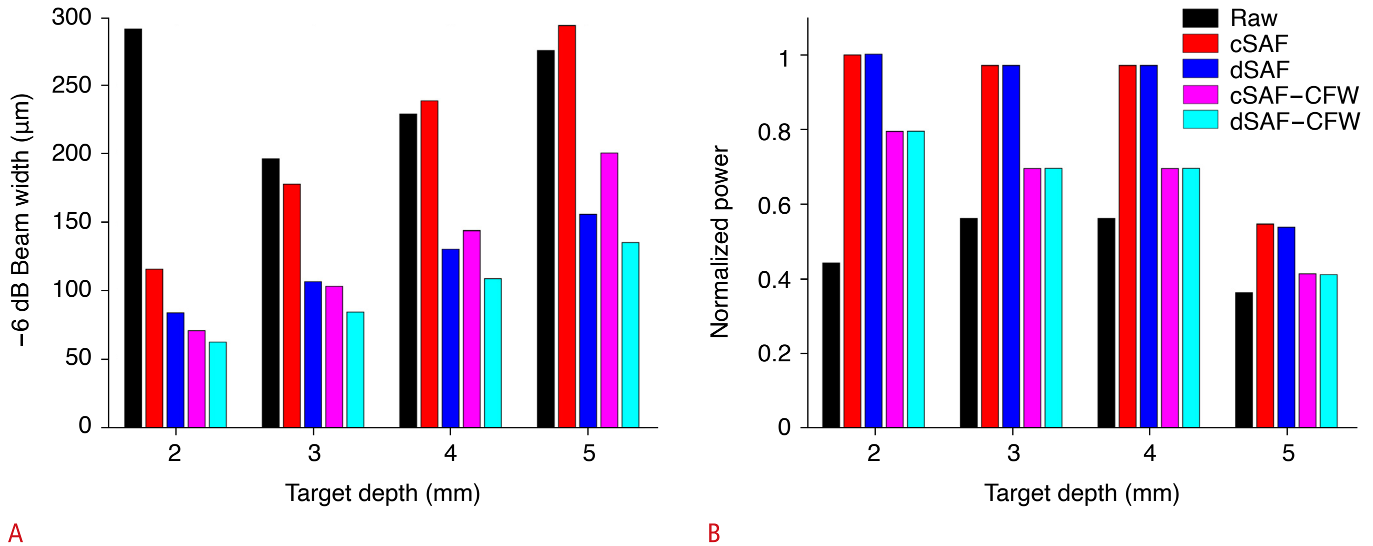

Fig. 7. Simulation summary: −6 dB lateral beamwidths and normalized peak magnitudes across depths.
A. The −6 dB lateral beamwidths for each method are summarized at various target depths. B. Relative peak magnitude at each target position is shown for the different reconstruction methods. cSAF, conventional synthetic aperture focusing; dSAF, directional SAF; CFW, coherence factor weighting.

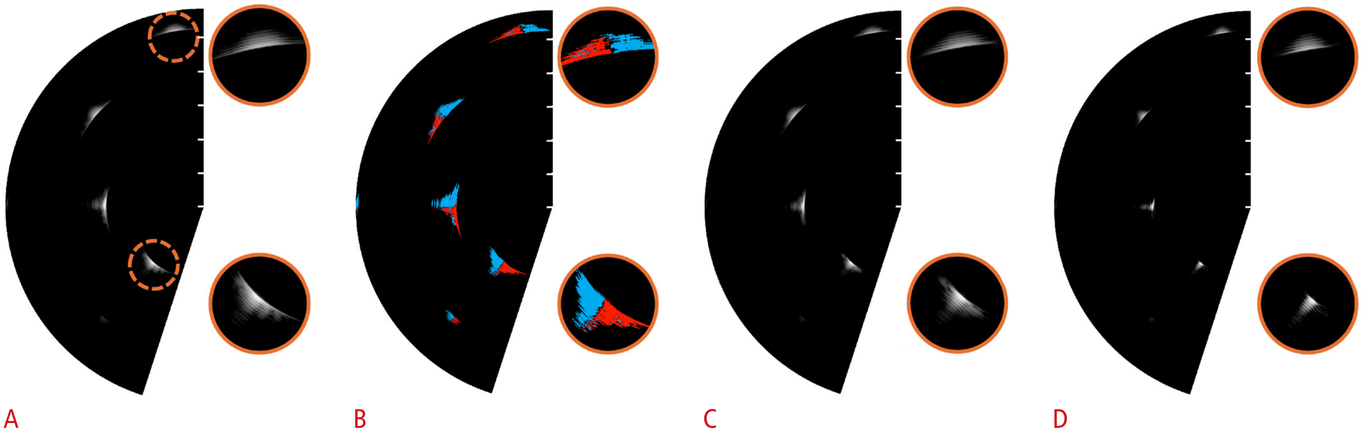

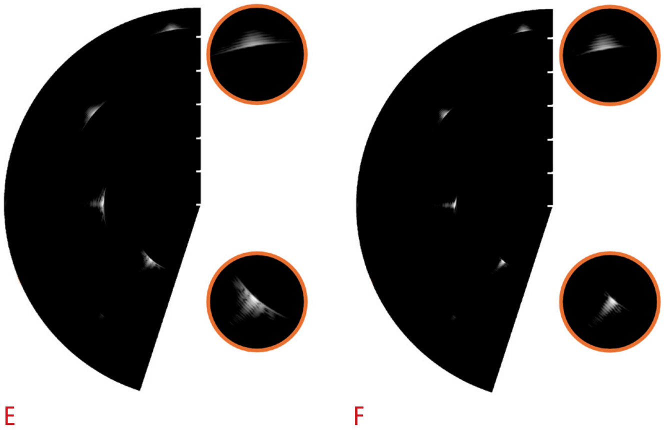

Fig. 8. Images of 25-μm gold wire targets at depths of 2, 3, 4, and 5 mm, obtained using different imaging methods.
Raw (A), estimated directional map (B), conventional synthetic aperture focusing (cSAF) (C), cSAF-coherence factor weighting (CFW) (D), directional (dSAF) (E), and dSAF-CFW (F) are shown. Magnified views of the targets at 2 mm and 5 mm (highlighted by yellow dashed circles) are shown beside the intravascular ultrasound images. All images were logarithmically compressed with a dynamic range of 50 dB. The white bars on the vertical axis indicate 1-mm intervals.

mm, 54 MHz) developed for this research was employed [6], and the entire setup was immersed in a deionized water bath. The transducer was mounted at the center of a rotational stage (SGSP160-YAW, Sigmakoki Co. Ltd.), which was rotated counterclockwise in 0.36° increments to acquire 1,000 scanlines. A pulser/receiver (UT340, UTEX Scientific Instruments Inc.) transmitted and amplified the signals, which were then digitized (CS12502, Gage Applied Technologies Inc.) and stored on a PC. All instrumentation was controlled via a custom LabVIEW program, and post-processing (beamforming, directional screening, and CFW) was performed in MATLAB (MathWorks Inc.) with the same parameters used in the simulations.

Fig. 8 shows representative images of the 25-μm gold wire target at depths of 2, 3, 4, and 5 mm. Fig. 8A presents the raw image, Fig. 8B displays the estimated directional map used in dSAF, and Fig. 8C–F illustrate cSAF, cSAF-CFW, dSAF, and dSAF-CFW, respectively. Each image was log-compressed with a 50-dB dynamic range, and magnified views of the targets at 2 and 5 mm (indicated by dashed yellow circles) are shown beside the IVUS images. As with the simulation study, the directional map clearly separates negative and positive phases around the wire center, enabling the proposed dSAF approach to eliminate off-axis signals more effectively than conventional cSAF.

To quantify spatial resolution, lateral beam profiles of the wire

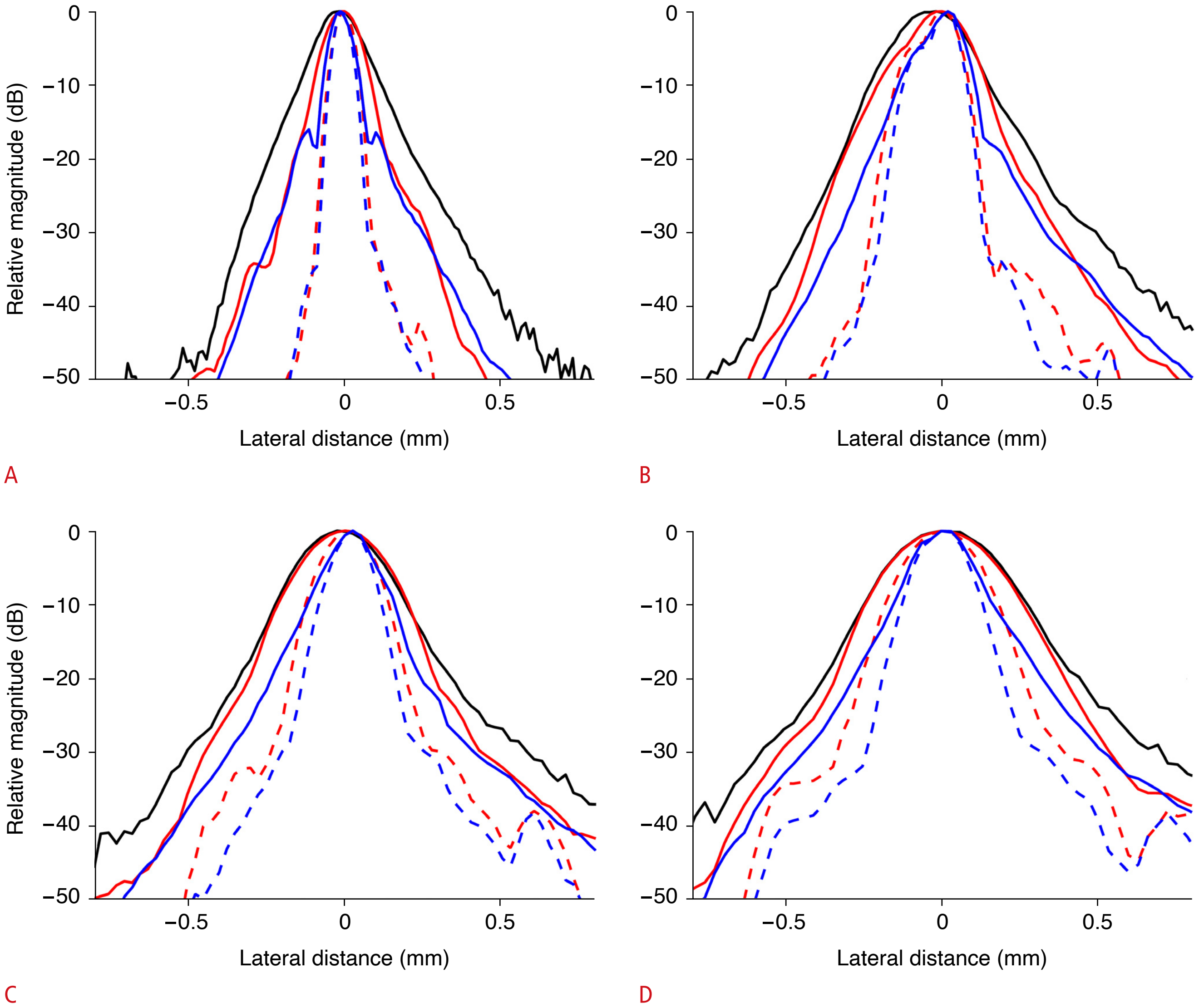

Fig. 9. Wire-phantom lateral beam profiles at 2–5 mm.

Lateral profiles at depths of 2 mm (A), 3 mm (B), 4 mm (C), and 5 mm (D) are obtained from the wire phantom images. The solid black line represents the raw data, the solid and dotted red lines correspond to conventional synthetic aperture focusing (cSAF) and cSAF-coherence factor weighting (CFW), and the solid and dotted blue lines indicate directional SAF (dSAF) and dSAF-CFW, respectively.

target at depths of 2, 3, 4, and 5 mm were extracted from each image and plotted in Fig. 9. The solid black lines represent the raw image, the solid and dotted red lines correspond to cSAF and cSAF-CFW, and the solid and dotted blue lines indicate dSAF and dSAF-CFW, respectively. Consistent with the simulation results, dSAF yielded narrower −6 dB beamwidths than cSAF across all depths. For instance, dSAF measured lateral beamwidths of 94.7, 181.2, 192, and 233.1 μm at 2, 3, 4, and 5 mm, whereas cSAF exhibited 145.3, 255.2, 321.8, and 397 μm. dSAF-CFW further refined these beamwidths to 73, 158.9, 151.4, and 206.9 μm, providing additional improvement over cSAF-CFW (86.3, 188, 210.2, and 279.3 μm). On average, the proposed dSAF-based methods surpassed the conventional methods (cSAF and cSAF-CFW) by 37.3% and 22.7%, respectively.

Fig. 10 shows the axial beam profiles at 2, 3, 4, and 5 mm, normalized to the maximum amplitude of the 2-mm target to evaluate any loss in penetration depth. Despite screening out off-axis echoes, dSAF maintained a relative peak magnitude similar to cSAF, indicating that its resolution gains do not come at the expense of reduced signal penetration. The same trend was observed for dSAF-CFW, which exhibited peak amplitudes comparable to those of cSAF-CFW.

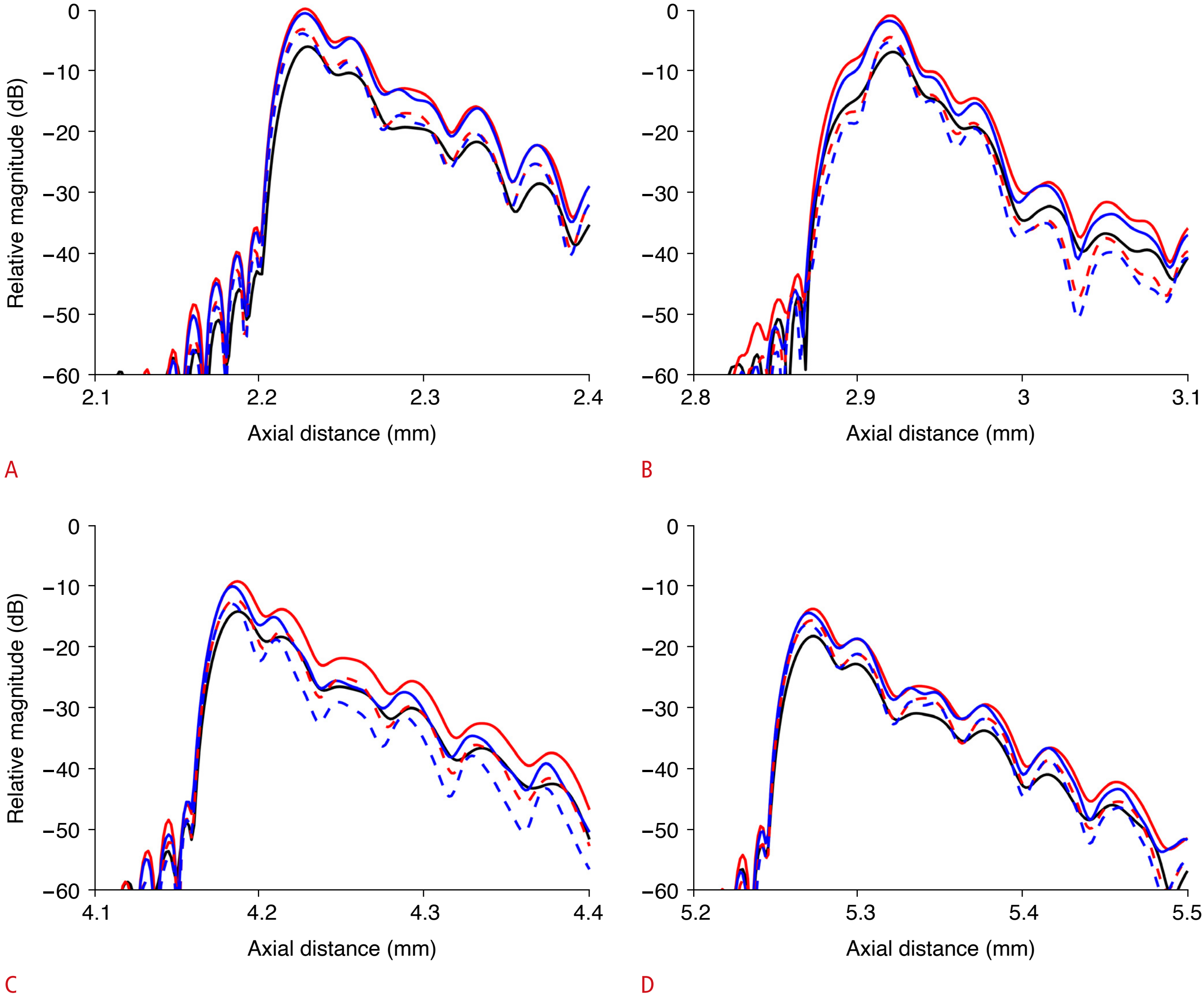

Fig. 10. **Wire-phantom axial beam profiles at 2–5 mm (penetration assessment).**
Axial profiles at depths of 2 mm (A), 3 mm (B), 4 mm (C), and 5 mm (D) are obtained from the wire phantom images. Magnitudes were normalized to the maximum value of the 2-mm target to assess any decrease in penetration depth. The solid black line represents the raw data, the solid and dotted red lines correspond to conventional synthetic aperture focusing (cSAF) and cSAF-coherence factor weighting (CFW), and the solid and dotted blue lines indicate directional SAF (dSAF) and dSAF-CFW, respectively.

Fig. 11A summarizes the −6 dB lateral beamwidths for each method at all wire target positions, reflecting the detailed profiles in Figs. 9 and 10. Meanwhile, Fig. 11B depicts the corresponding relative peak magnitudes, confirming that neither dSAF nor dSAF-CFW compromises signal intensity compared with cSAF or cSAF-CFW. Overall, these findings indicate that the proposed dSAF approach significantly enhances lateral resolution without degrading imaging depth, even when fewer synthetic scanlines are used. Notably, dSAF achieves performance comparable to or better than cSAF-CFW, while avoiding some of the gain reduction and artifact issues typically associated with CFW.

Because the number of scanlines influences SAF performance, cSAF-CFW was evaluated while varying the number of synthesized scanlines and compared with the proposed dSAF-CFW. The depth-adaptive baseline used N=39/27/19/15 synthesized scanlines at depths of 2/3/4/5 mm (aperture size=1.0); this was scaled to 1.5 (57/39/27/21) and 0.5 (19/13/9/7). As shown in Fig. 12, increasing the cSAF aperture narrows the −6 dB beamwidth, whereas reducing it broadens the mainlobe; nevertheless, dSAF-CFW consistently yields equal or smaller beamwidths and suppresses sidelobes. These findings indicate that the advantage of the proposed directional-gating approach is robust to changes in the amount of aggregated RF data, confirming superiority over conventional cSAF strategies across a range of synthesized apertures.

In addition to the wire phantom study, a custom tissue-mimicking phantom containing three cysts (approximately 1 mm in diameter) was used to evaluate contrast performance. Fig. 13 presents representative images obtained with five approaches: A, raw; B, cSAF; C, dSAF; D, cSAF-CFW; and E, dSAF-CFW. Each image was reconstructed with a 50-dB dynamic range. The three cyst targets were embedded at depths of approximately 2, 3, and 4 mm, enabling a multi-depth contrast assessment.

To quantify contrast improvements, the CNR was computed for each method by selecting cyst and background regions of interest (ROIs), as illustrated in Fig. 14A. The size of each ROI was approximately 0.5 mm×0.5 mm for both the cystic region and the surrounding background. The resulting CNR values (Fig. 14B) show that the proposed dSAF method provides higher contrast than both cSAF and the raw images across all cyst depths, with the dSAF-CFW variant offering additional sidelobe suppression in some instances. However, slight gain reduction may occur with CFW, consistent with the findings from the wire phantom and simulation studies.

Overall, these phantom images confirm that integrating echo directional screening (dSAF) significantly improves contrast in cystic regions while maintaining uniform background speckle. The ability to enhance contrast without compromising penetration depth or introducing excessive artifacts underscores the viability of dSAF-based approaches for more detailed and reliable IVUS imaging of vascular structures.

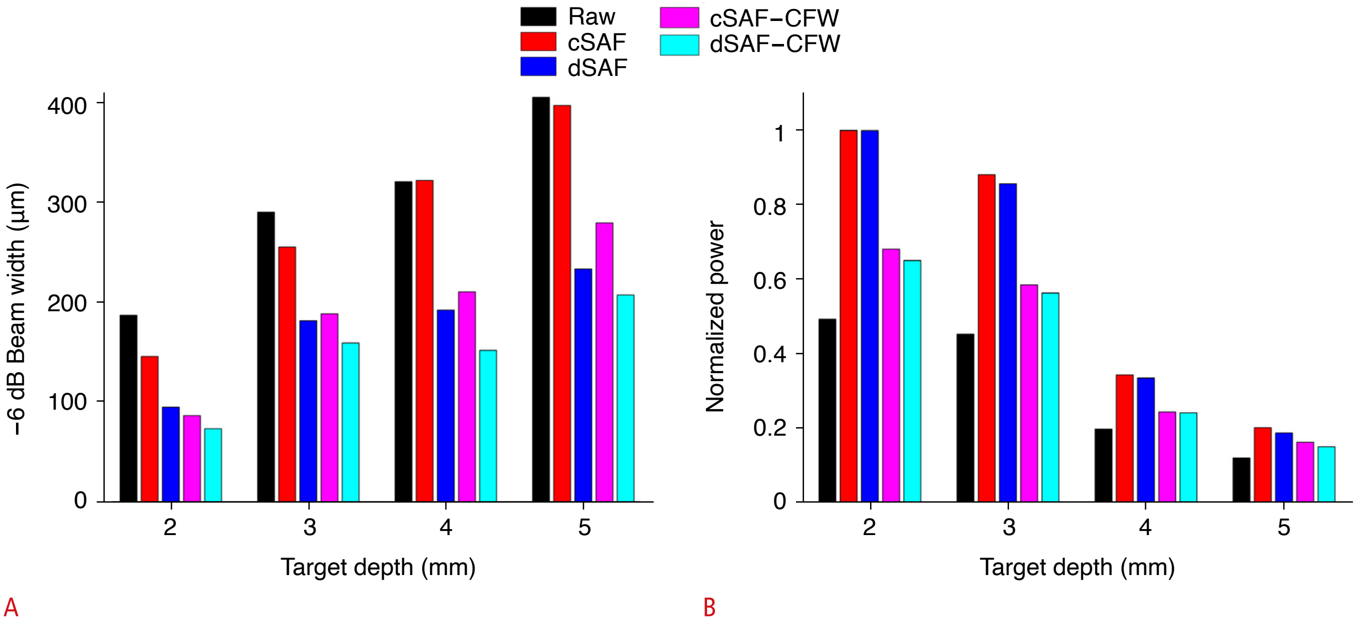

Fig. 11. Wire-phantom summary: −6 dB lateral beamwidths and normalized peak magnitudes.

A. Measured −6 dB lateral beamwidths are obtained from the wire phantom lateral profiles at each target position for each method. B. Relative peak magnitude is derived from the axial profiles at each target position for each method. cSAF, conventional synthetic aperture focusing; dSAF, directional SAF; CFW, coherence factor weighting.

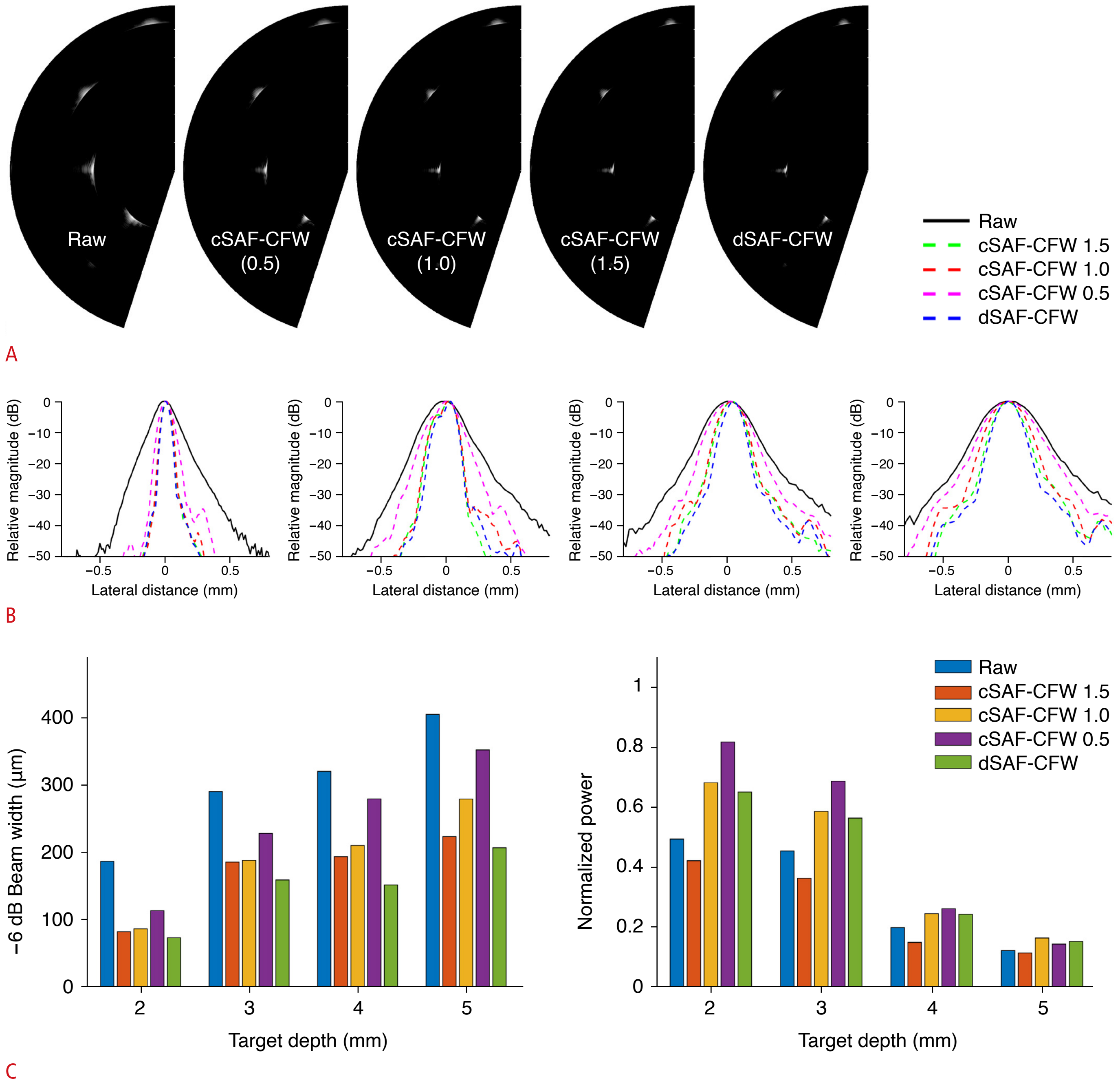

Fig. 12. Effect of the number of synthesized scanlines (aperture size) on wire target imaging.
A. Intravascular ultrasound images reconstructed as follows: raw, conventional synthetic aperture focusing (cSAF)-coherence factor weighting (CFW) (0.5), cSAF-CFW (1.0), cSAF-CFW (1.5), and directional SAF (dSAF)-CFW. To account for the depth-dependent radiation pattern, the number of synthesized scanlines was adapted with depth; for 2/3/4/5 mm, N was 39/27/19/15 in the baseline (aperture_size = 1.0) and was scaled to 57/39/27/21 for 1.5 and 19/13/9/7 for 0.5. B. Lateral beam profiles (normalized to each peak) at 2, 3, 4, and 5 mm are shown; colors/line styles follow the legend (raw, solid black; cSAF-CFW 1.5/1.0/0.5, dashed green/red/magenta; dSAF-CFW, dashed blue). C. Summary metrics across depths are shown: −6 dB beamwidth (left) and normalized power (right). Across all depths, dSAF-CFW produces a narrower mainlobe that is comparable to or better than cSAF-CFW even when the aperture size is varied.

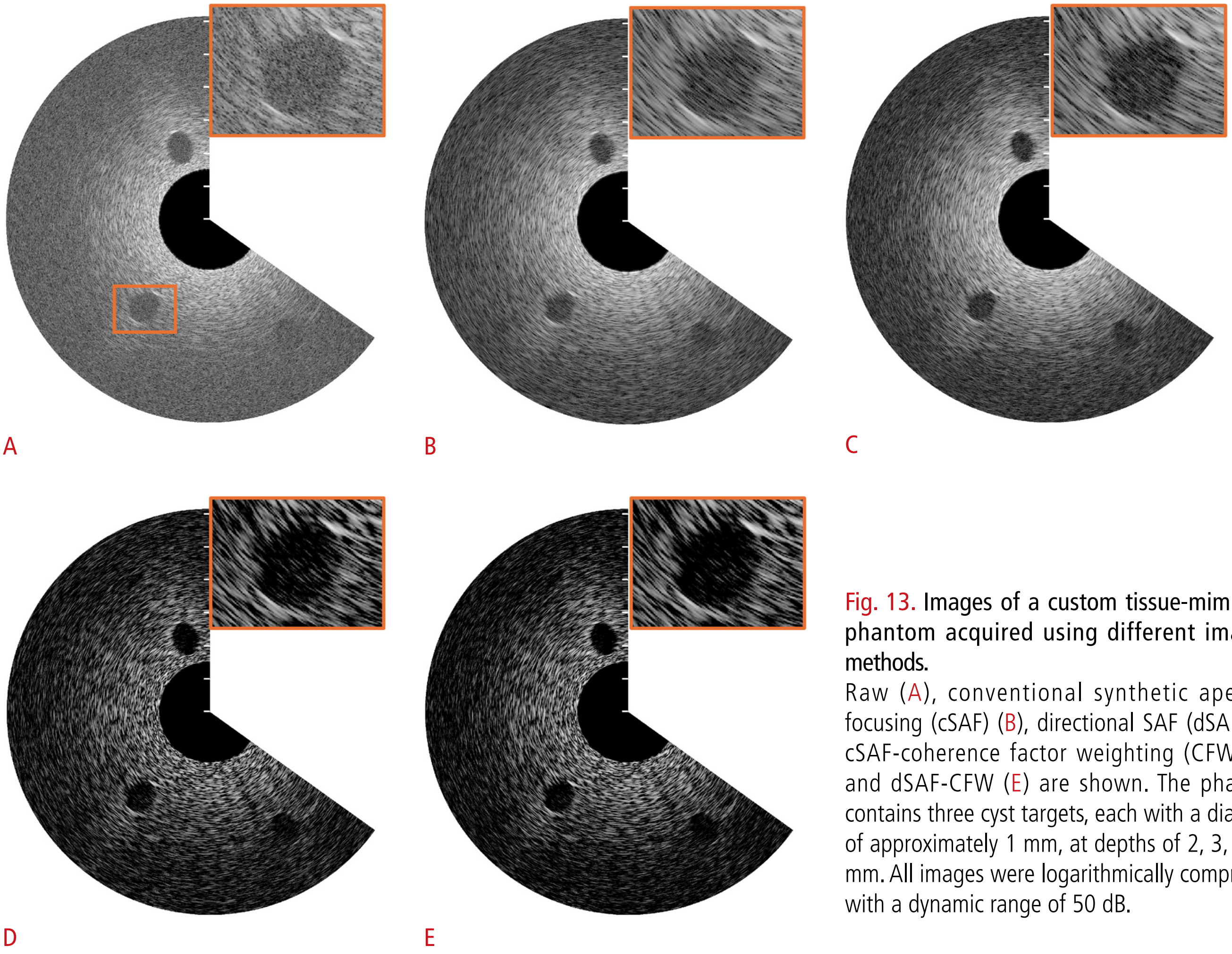

Fig. 13. **Images of a custom tissue-mimicking phantom acquired using different imaging methods.**
Raw (A), conventional synthetic aperture focusing (cSAF) (B), directional SAF (dSAF) (C), cSAF-coherence factor weighting (CFW) (D), and dSAF-CFW (E) are shown. The phantom contains three cyst targets, each with a diameter of approximately 1 mm, at depths of 2, 3, and 4 mm. All images were logarithmically compressed with a dynamic range of 50 dB.

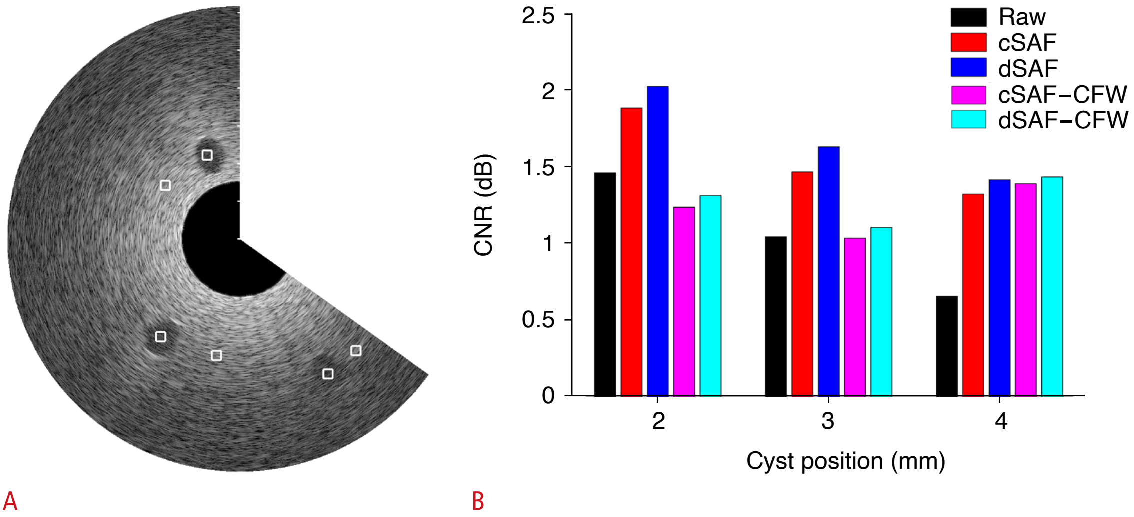

Fig. 14. **Cyst-phantom contrast-to-noise ratio (CNR) analysis: regions of interest (ROI) placement and CNR comparisons across methods.** A. ROIs (highlighted by white rectangles) for the cyst and background at depths of 2, 3, and 4 mm are shown in a representative cyst phantom image. These ROIs were used to calculate the CNR for each imaging method. B. Estimated CNR results for each method are obtained based on the ROIs in A. CNR was evaluated on images reconstructed with five methods: raw, conventional synthetic aperture focusing (cSAF), directional SAF (dSAF), cSAF-coherence factor weighting (CFW), and dSAF-CFW.

Discussion

This study demonstrates that dSAF can overcome key limitations of cSAF in IVUS imaging. By explicitly tracking echo direction via phase analysis and screening out off-axis signals, dSAF prevents the contamination that occurs when cSAF assumes uniform time-of-flight delays for all incoming echoes. Both simulation and phantom results confirm that dSAF significantly narrows the −6 dB beamwidth, thereby improving spatial resolution at depths from 2 mm to 5 mm. Moreover, penetration depth is preserved, as indicated by peak magnitudes comparable to those of cSAF. Although CFW can further refine resolution through sidelobe suppression, it may introduce gain-reduction artifacts near hyperechoic targets; notably, the resolution of dSAF alone often equals or surpasses cSAF-CFW, obviating the need for additional post-processing and its potential drawbacks.

Several considerations warrant investigation to fully integrate dSAF into clinical IVUS workflows. First, *in vivo* testing is critical, especially under non-uniform rotational distortion and catheter pullback motion, where the ideal assumptions about transducer rotation and angular sampling are less reliable. Although earlier studies suggest some tolerance for random rotation errors, real catheter motion may deviate substantially from nominal conditions, necessitating robust correction mechanisms. Second, the beam shape of the IVUS transducer must be carefully considered, as in geometrically focused designs where the wavefront transitions from convex to concave across the focal region. In such scenarios, an adaptive directional mask (e.g., applying an inverse sign in the far field) must be developed to maintain accurate echo screening. Third, advanced adaptive imaging methods based on deep neural networks may complement dSAF, particularly for real-time parameter tuning and dynamic beamforming [35]. Integrating similar approaches with dSAF could further improve image clarity and reduce artifacts, even in complex IVUS environments. For deep learning-based methods, a further challenge lies in the computational overhead when deployed in practice, which can be mitigated by hardware acceleration techniques [36,37].

A novel dSAF framework has been introduced for single-element, rotational IVUS imaging, incorporating phase-based directional maps to exclude off-axis echoes. The effectiveness of this method was verified through PSF simulations and phantom experiments, revealing notable improvements in lateral resolution (up to 37.3% in wire phantom testing) and contrast (up to an 8.6% gain in CNR) without degrading penetration depth. By enabling high-resolution IVUS imaging without heavy reliance on CFW and its associated artifacts, dSAF holds potential for more accurate identification of critical vascular features such as thin fibrous caps. Future work will explore the method's *in vivo* performance, particularly under non-uniform rotational distortion and pullback motion.

ORCID: Hyunwoo Cho: https://orcid.org/0000-0003-3063-8833; Jin Ho Chang: https://orcid.org/0000-0002-8323-4202; Jihun Jang: https://orcid.org/0000-0002-8179-9410; Yangmo Yoo: https://orcid.org/0000-0001-8952-6444

Author Contributions

Conceptualization: Chang JH, Jang J, Yoo Y. Data acquisition: Cho H, Lee J, Chang JH. Data analysis or interpretation: Cho H, Lee J, Park D, Jang J, Yoo Y. Drafting of the manuscript: Cho H, Lee J, Jang J, Yoo Y. Critical revision of the manuscript: Cho H, Park D, Chang JH, Jang J, Yoo Y. Approval of the final version of the manuscript: all authors.

Conflict of Interest

No potential conflict of interest relevant to this article was reported.

References

1. Gaidai O, Cao Y, Loginov S. Global cardiovascular diseases death rate prediction. Curr Probl Cardiol 2023;48:101622.
2. Roth GA, Mensah GA, Johnson CO, Addolorato G, Ammirati E, Baddour LM, et al. Global burden of cardiovascular diseases and risk factors, 1990-2019: update from the GBD 2019 study. J Am Coll Cardiol 2020;76:2982-3021.
3. Garcia-Garcia HM, Costa MA, Serruys PW. Imaging of coronary atherosclerosis: intravascular ultrasound. Eur Heart J 2010;31:2456-2469.
4. Fujii K, Hao H, Ohyanagi M, Masuyama T. Intracoronary imaging for detecting vulnerable plaque. Circ J 2013;77:588-595.
5. Elliott MR, Thrush AJ. Measurement of resolution in intravascular ultrasound images. Physiol Meas 1996;17:259-265.
6. Lee J, Jang J, Chang JH. Oblong-shaped-focused transducers for intravascular ultrasound imaging. IEEE Trans Biomed Eng 2017;64:671-680.
7. Garcia-Guimaraes M, Cuesta J, Rivero F, Bastante T, Benedicto A, Alfonso F. High-definition intravascular ultrasound vs optical coherence tomography: preliminary experience. Rev Esp Cardiol (Engl Ed) 2018;71:119-120.
8. Qiu W, Wang X, Chen Y, Fu Q, Su M, Zhang L, et al. Modulated excitation imaging system for intravascular ultrasound. IEEE Trans Biomed Eng 2017;64:1935-1942.
9. Ma T, Yu M, Li J, Munding CE, Chen Z, Fei C, et al. Multi-frequency intravascular ultrasound (IVUS) imaging. IEEE Trans Ultrason Ferroelectr Freq Control 2015;62:97-107.
10. Munding CE, Cherin E, Jourard I, Weyers JJ, Goertz DE, Courtney BK, et al. Development of a 3 French dual-frequency intravascular ultrasound catheter. Ultrasound Med Biol 2018;44:251-266.
11. Lee HS, Jeong JS. Triple-element back-to-back transducer with 3D

printed housing for intravascular ultrasound imaging: a feasibility study. IEEE Access 2022;10:9287-9297.

12. Su M, Zhang Z, Hong J, Huang Y, Mu P, Yu Y, et al. Cable shared dual-frequency catheter for intravascular ultrasound. IEEE Trans Ultrason Ferroelectr Freq Control 2019;66:849-856.
13. Frijlink ME, Goertz DE, van Damme LC, Krams R, van der Steen AF. Intravascular ultrasound tissue harmonic imaging in vivo. IEEE Trans Ultrason Ferroelectr Freq Control 2006;53:1844-1852.
14. Cherin EW, Poulsen JK, van der Steen AF, Lum P, Foster FS. Experimental characterization of fundamental and second harmonic beams for a high-frequency ultrasound transducer. Ultrasound Med Biol 2002;28:635-646.
15. van der Steen AF, Poulsen JK, Cherin E, Foster FS. Harmonic imaging at high frequencies for IVUS. In: Proceedings of the IEEE Ultrasonics Symposium; 1999 Oct 17-20; Tahoe, NV, USA. Piscataway, NJ: Institute of Electrical and Electronics Engineers, 1999;1537-1540.
16. Frijlink ME, Goertz DE, Foster FS, van der Steen AF. High frequency harmonic imaging in presence of intravascular stents. In: Proceedings of the IEEE Ultrasonics Symposium; 2003 Oct 5-8; Honolulu, HI, USA. Piscataway, NJ: Institute of Electrical and Electronics Engineers, 2003;208-211.
17. Lee J, Chang JH. Dual-element intravascular ultrasound transducer for tissue harmonic imaging and frequency compounding: development and imaging performance assessment. IEEE Trans Biomed Eng 2019;66:3146-3155.
18. Lee J, Moon JY, Chang JH. A 35 MHz/105 MHz dual-element focused transducer for intravascular ultrasound tissue imaging using the third harmonic. Sensors (Basel) 2018;18:2290.
19. Jang J, Chang JH. Design and fabrication of a miniaturized convex array for combined ultrasound and photoacoustic imaging of the prostate. IEEE Trans Ultrason Ferroelectr Freq Control 2018;65:2086-2096.
20. Cha JH, Kang B, Jang J, Chang JH. A 15-MHz 1-3 piezocomposite concave array transducer for ophthalmic imaging. IEEE Trans Ultrason Ferroelectr Freq Control 2015;62:1994-2004.
21. Cha JH, Chang JH. Development of 15 MHz 2–2 piezo-composite ultrasound linear array transducers for ophthalmic imaging. Sens Actuators A Phys 2014;217:39-48.
22. Frazier CH, O'Brien WR. Synthetic aperture techniques with a virtual source element. IEEE Trans Ultrason Ferroelectr Freq Control 1998;45:196-207.
23. Kim C, Yoon C, Park JH, Lee Y, Kim WH, Chang JM, et al. Evaluation of ultrasound synthetic aperture imaging using bidirectional pixel-based focusing: preliminary phantom and in vivo breast study. IEEE Trans Biomed Eng 2013;60:2716-2724.
24. Li ML, Guan WJ, Li PC. Improved synthetic aperture focusing technique with applications in high-frequency ultrasound imaging. IEEE Trans Ultrason Ferroelectr Freq Control 2004;51:63-70.
25. Cai D, Li G, Xia D, Li Z, Guo Z, Chen SL. Synthetic aperture focusing technique for photoacoustic endoscopy. Opt Express 2017;25:20162-20171.
26. Vray D, Haas C, Rastello T, Krueger M, Brusseau E, Schroeder K, et al. Synthetic aperture-based beam compression for intravascular ultrasound imaging. IEEE Trans Ultrason Ferroelectr Freq Control 2001;48:189-201.
27. Asl BM, Mahloojifar A. Minimum variance beamforming combined with adaptive coherence weighting applied to medical ultrasound imaging. IEEE Trans Ultrason Ferroelectr Freq Control 2009;56:1923-1931.
28. Liao CK, Li ML, Li PC. Optoacoustic imaging with synthetic aperture focusing and coherence weighting. Opt Lett 2004;29:2506-2508.
29. Yu M, Li Y, Ma T, Shung KK, Zhou Q. Intravascular ultrasound imaging with virtual source synthetic aperture focusing and coherence factor weighting. IEEE Trans Med Imaging 2017;36:2171-2178.
30. Opretzka J, Vogt M, Ermert H. A synthetic aperture focusing technique with optimized beamforming for high-frequency ultrasound. In: Proceedings of the IEEE Ultrasonics Symposium; 2010 Oct 11-14; San Diego, CA, USA. Piscataway, NJ: Institute of Electrical and Electronics Engineers, 2011;2303-2306.
31. Wang Y, Peng H, Zheng C, Han Z, Qiao H. A dynamic generalized coherence factor for side lobe suppression in ultrasound imaging. Comput Biol Med 2020;116:103522.
32. Kang S, Lee J, Chang JH. Effectiveness of synthetic aperture focusing and coherence factor weighting for intravascular ultrasound imaging. Ultrasonics 2021;113:106364.
33. Karaman M, Li PC, O'Donnell M. Synthetic aperture imaging for small scale systems. IEEE Trans Ultrason Ferroelectr Freq Control 1995;42:429-442.
34. Kasai C, Namekawa K, Koyano A, Omoto R. Real-time two-dimensional blood flow imaging using an autocorrelation technique. IEEE Trans Sonics Ultrason 1985;32:458-464.
35. Cho H, Park S, Kang J, Yoo Y. Deep coherence learning: an unsupervised deep beamformer for high quality single plane wave imaging in medical ultrasound. Ultrasonics 2024;143:107408.
36. Cho H, Song I, Jang J, Yoo Y. A lightweight deep learning network on a system-on-chip for wearable ultrasound bladder volume measurement systems: preliminary study. Bioengineering (Basel) 2023;10:525.
37. Cho H, Kim D, Chang S, Kang J, Yoo Y. A system-on-chip solution for deep learning-based automatic fetal biometric measurement. Expert Syst Appl 2024;237:121482.